

Journal of Biomedical Optics

BiomedicalOptics.SPIEDigitalLibrary.org

Assessment of microcirculation dynamics during cutaneous wound healing phases *in vivo* using optical microangiography

Siavash Yousefi
Jia Qin
Suzan Dziennis
Ruikang K. Wang

Assessment of microcirculation dynamics during cutaneous wound healing phases *in vivo* using optical microangiography

Siavash Yousefi, Jia Qin, Suzan Dziennis, and Ruikang K. Wang*

University of Washington, Department of Bioengineering, Seattle, Washington 98195, United States

Abstract. Cutaneous wound healing consists of multiple overlapping phases starting with blood coagulation following incision of blood vessels. We utilized label-free optical coherence tomography and optical microangiography (OMAG) to noninvasively monitor healing process and dynamics of microcirculation system in a mouse ear pinna wound model. Mouse ear pinna is composed of two layers of skin separated by a layer of cartilage and because its total thickness is around 500 μm , it can be utilized as an ideal model for optical imaging techniques. These skin layers are identical to human skin structure except for sweat ducts and glands. Microcirculatory system responds to the wound injury by recruiting collateral vessels to supply blood flow to hypoxic region. During the inflammatory phase, lymphatic vessels play an important role in the immune response of the tissue and clearing waste from interstitial fluid. In the final phase of wound healing, tissue maturation, and remodeling, the wound area is fully closed while blood vessels mature to support the tissue cells. We show that using OMAG technology allows noninvasive and label-free monitoring and imaging each phase of wound healing that can be used to replace invasive tissue sample histology and immunochemistry technologies. © 2014 Society of Photo-Optical Instrumentation Engineers (SPIE) [DOI: [10.1117/1.JBO.19.7.076015](https://doi.org/10.1117/1.JBO.19.7.076015)]

Keywords: optical coherence tomography; optical microangiography; wound healing; lymph; mouse ear pinna.

Paper 140185R received Mar. 19, 2014; revised manuscript received May 24, 2014; accepted for publication Jun. 5, 2014; published online Jul. 18, 2014.

1 Introduction

Cutaneous wounds are usually created as a result of damage to the skin due to injury that can lead to disability or death in some cases such as burns, chronic skin ulcers, and diabetes mellitus.¹ Natural wound healing consists of overlapping multiphase processes including hemostasis, inflammation, tissue formation, and tissue remodeling. If the skin is not perfectly healed as it was before the injury, scar tissue is formed. The hairless mouse ear pinna model has been extensively used for *in vivo* studies of the skin microcirculation.² Mouse ear pinna is composed of two layers of skin separated by a layer of cartilage. Because of its relatively thin structure ($\sim 500 \mu\text{m}$), optical imaging techniques can be utilized to noninvasively image microcirculation within the pinna tissue. These skin layers are almost identical to human skin structure except for sweat ducts and glands.³

Optical coherence tomography (OCT) is a noncontact technique based on light backscattering properties of the tissue structures.^{4,5} OCT is analogous to ultrasound tomography. Similar to ultrasound Doppler modes, OCT hemodynamic information can be acquired in addition to structure information. Compared to ultrasound imaging, OCT resolution is higher ($<10 \mu\text{m}$) while the penetration and imaging depth are limited ($<2 \text{ mm}$). Utilizing the dynamic OCT signals (speckle) induced by moving blood cells within patent vessels, optical microangiography (OMAG) is developed to obtain three-dimensional (3-D) blood perfusion map in microcirculatory tissue beds *in vivo* using Fourier domain OCT.^{6,7} There exist numerous techniques for OMAG processing from OCT

signals such as absolute value frame subtraction,^{8,9} correlation mapping OCT,¹⁰ correlation masking,¹¹ split spectrum amplitude decorrelation,¹² cross-sectional filters,¹³ and eigen-regression filters.¹⁴

Wound healing models in mice are very popular among researchers because mice are inexpensive, easy to handle, available in large numbers, and have low risk of death under anesthesia.¹⁵ Most of the existing models of wound healing studies are performed in mice with specific gene knocked out, followed by immunohistochemistry and histology.¹⁶ Development of noninvasive methods for the monitoring of wound healing can help the researchers to better understand the mechanisms and effect of therapeutic treatment on healing process in chronic and diabetic wound diseases. Wound healing and microvasculature remodeling in the mouse ear pinna model has been previously studied using OMAG¹⁷ and laser speckle imaging.¹⁸ Briefly, a biopsy punch is performed on one of the major artery/vein pairs of the ear. The initial tissue response to the wound is triggered immediately after the punch by blood coagulation, recruiting peripheral capillaries, and redirection of main arterial/venous blood flow. During the healing process, the wound size is gradually reduced with time and the wound surface is fully closed within 4 weeks. However, microcirculation and capillary maturation continue for months. In this paper, we demonstrate the capability of OMAG to describe in detail the microcirculation response including capillaries, large vessels, and lymphatic vessels during wound healing phases.

*Address all correspondence to: Ruikang K. Wang, E-mail: wangrk@uw.edu

2 Experimental Setup

2.1 OCT System Setup and Scanning Protocol

Noninvasive *in vivo* images were acquired from the pinna of a healthy ~6-week-old male hairless mouse (CrI:SKH1-Hr^{hr}) weighing approximately 25 g. During this experiment, the mouse was anesthetized using 2% isoflurane (0.2 L/min O₂, 0.8 L/min air). The ear was kept flat on a microscope glass using removable double-sided tape. The experimental protocol was in compliance with the federal guidelines for care and handling of small rodents and approved by the Institution Animal Care and Use Committee of the University of Washington, Seattle.

In this study, we used a spectral domain OCT (SD-OCT) system to implement the OMAG. The schematic of the SD-OCT system is shown in Fig. 1(a), in which the light source was a superluminescent diode (SLD, DenseLight, Singapore) with the center wavelength of 1310 nm and a bandwidth of 65 nm. This light source gave an axial resolution of ~12 μm in the air. An optical circulator (OC) was used to couple the light from the SLD into fiber-based Michelson interferometer. In the reference arm of the interferometer, a stationary mirror was utilized after polarization controller. In the sample arm of the interferometer, a microscopy objective lens with 18-mm focal length was used to achieve ~5.8-μm lateral resolution. The backscattered light from the sample and the reflected light from the reference mirror were recombined at the 2 × 2 optical fiber coupler. Since the wavelength of the light source is invisible to the human eye, a 633-nm laser diode was used as a guiding beam to locate the imaging position. This guiding beam helps to adjust the sample under the OCT system and image the desired location. The recombined light was then routed to a home-built high-speed spectrometer via the OC (AC Photonics, Santa Clara, California). In the design of the spectrometer, a collimator with the focal length of 30 mm and a 14-bit, 1024-pixel InGaAs linescan camera (SUI, Goodrich Corp., Akron, Ohio) were used. The camera speed was 47,000 lines/s. The spectral resolution of the designed spectrometer was ~0.141 nm that provided a detectable depth

range of 3.0 mm on each side of the zero-delay line. The system had a measured signal-to-noise ratio of 105 dB with a light power on the sample at ~3 mW. Figure 1(b) shows a photograph of a mouse ear pinna before inducing biopsy punch taken by a digital camera, in which the area marked by the rectangular box gives a typical field-of-view and scanning range for OMAG/OCT system, which is 2.2 × 2.2 mm² in the current setup. In order to scan a larger field on the ear, we used a mechanical translating stage to move the tissue sample to the desired location and after acquisition and processing, the mosaics were stitched together to form a larger image.

The scanning protocol was based on 3-D ultrahigh-sensitive optical microangiography (UHS-OMAG) technique that requires acquisition of multiple B-scans at the same spatial location and then shifting the slow-scanning mirror to the adjacent cross section.^{19,20} The x-scanner (fast B-scan) was driven with a sawtooth waveform, and the y-scanner (slow C-scan) was driven with a step function waveform. The fast and slow scanners covered a rectangular area of ~2.2 × 2.2 mm² on the sample. Each B-scan consisted of 400 A-lines covering a range of ~2.2 mm on the sample. The duty cycle of the sawtooth waveform rising edge was set at ~80%/cycle, which provided a B-scan frame rate of ~94 frames/s. The C-scan consisted of 400 scan locations with B-scan repetition of 8 frames/location for flow imaging and quantification. The total size of the data set was 1.28 × 10⁶ A-lines. In order to cover a large field-of-view, multiple overlapping 3-D scans were acquired and the sample was translated using a mechanical stage. This allowed imaging a large area on the mouse ear pinna.

The acquired data were transferred to a personal computer and processed off-line using an m-file code developed on MATLAB® (The Mathworks Inc., Natick, Massachusetts). The processing consists of removing interference signal from reference arm, dispersion correction, resampling each A-line from nonlinear wavelength space to the linear K-space, and applying fast Fourier transform (FFT).²¹ The FFT amplitude of the repeated B-scans at the same spatial location was averaged temporally to generate structure cross-section images. The procedures to map blood flow perfusion and lymphatic vessels are explained below.

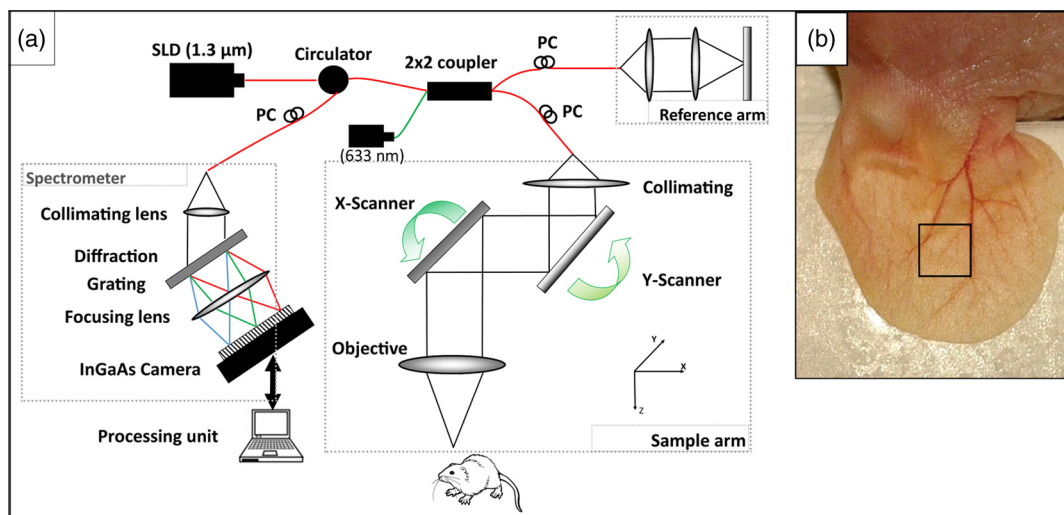


Fig. 1 (a) Schematic diagram of the imaging system. (b) Typical mouse ear pinna flattened on the imaging platform. The biopsy punch size is 1 mm. The rectangular box shows typical scanning size of about 2.2 × 2.2 mm².

2.2 Blood Flow Perfusion Mapping Using OMAG

After OCT A-line reconstruction, OCT complex signal was utilized to generate blood flow perfusion. The details of this procedure were previously presented¹⁴ and here, we will briefly revisit the process. Repeated measured A-lines at each spatial location were utilized to get blood flow perfusion map within the structure. A matrix

$$X = [X(1), X(2), \dots, X(N)] \quad (1)$$

is formed by placing repeated A-lines at each spatial location where $X(i)$, $i = 1, \dots, N$ is an A-line vector. We assume that each received A-line from a biological sample (X) can be modeled by superposition of independent complex Gaussian random processes from stationary tissue structures or clutter (c), moving red blood cells (b), and noise (n) (combination of shot noise, quantization noise, and other nonlinearities in the imaging pipeline). Therefore, we can write

$$X = c + b + n. \quad (2)$$

Since these components are independent, X is also a Gaussian random process that can be completely characterized by its correlation matrix²²

$$R_x = R_c + R_b + \sigma_n^2 I, \quad (3)$$

where R_c is the clutter correlation matrix, R_b is the blood correlation matrix, σ_n^2 is the noise variance, and I is the identity matrix. Assuming that clutter is the dominant signal and its characteristics are similar along the depth, spatial average of the correlation of the received signal along the axial direction is an estimate of the clutter correlation matrix R_c given by

$$\hat{R}_c = \frac{1}{N} \sum_{i=1}^N \hat{R}_{ci} = \frac{1}{N} \sum_{i=1}^N X_i X_i^H. \quad (4)$$

The estimated correlation matrix \hat{R}_c can be decomposed into its corresponding eigenvalues and eigenvectors given by

$$\hat{R}_c = E \Lambda E^H, \quad (5)$$

where $E = [e_1, \dots, e_N]$ is the $N \times N$ unitary matrix of eigenvectors, $\Lambda = \text{diag}\{\lambda_1, \lambda_2, \dots, \lambda_N\}$ is the $N \times N$ diagonal matrix of eigenvalues and $\lambda_1 \geq \lambda_2 \geq \dots \geq \lambda_N = \sigma_n^2$ and σ_n^2 is the noise variance. We have shown⁹ that clutter subspace can be modeled by the first two components and therefore by removing the first two eigenvectors corresponding to the largest eigenvalues, we can get blood flow perfusion map using eigen-regression filter given by

$$Y = \left(I - \sum_{i=1}^2 e_i e_i^H \right) X, \quad (6)$$

where Y is clutter removed signal. Blood perfusion map for each A-line can be acquired by performing temporal mean and log compression on Y .

2.3 Segmentation of Lymphatic Vessels

Since the lymph fluid is clear and transparent, lymphatic vessels appear as reduced scattering (background noise level) vessel-

like areas in OCT structure cross-section images. The origin of these reduced-scattering connected tubular structures in the skin has been already confirmed by intradermal injection of Evan's blue dye and monitoring the uptake path by surrounding lymph vessels into the sentinel lymph node.²³ Therefore, these lymph vessels can be visualized by a proper segmentation algorithm on OCT structure images. The details of our segmentation algorithm were previously published²⁴ and here, we will briefly explain the process.

The local behavior of an image $I(x, s)$ at scale s and location x can be expressed by its Taylor series expansion up to second order given by

$$I(x + \delta x, s) \approx I(x, s) + \delta x^T \nabla(I)_s + \delta x^T H(I)_s \delta x, \quad (7)$$

where $\nabla(\cdot)_s$ and $H(\cdot)_s$ are the gradient vector and Hessian matrix of the image at scale s , respectively. Since our volume cross-section images are discrete signals, finding their two-dimensional first-order and second-order derivatives can be ill-posed. Using the concepts of linear scale space theory, differentiation can be defined as a convolution with derivatives of a Gaussian:

$$\frac{\partial}{\partial x} I(x, s) = s^\gamma I(x, s) * \frac{\partial}{\partial x} G(x, s), \quad (8)$$

where

$$G(x, s) = \frac{1}{\sqrt{2\pi s^2}} e^{-\frac{\|x\|^2}{2s^2}}, \quad (9)$$

where γ is the derivative normalization parameter and $\|\cdot\|$ is the Euclidean norm operation. The second-order derivative can be expressed as

$$\begin{aligned} \delta x^T H(I)_s \delta x &= \left(\frac{\partial}{\partial x} \right) \left(\frac{\partial}{\partial x} \right) I(x, s) \\ &= s^{2\gamma} I(x, s) * \frac{\partial^2}{\partial x^2} G(x, s). \end{aligned} \quad (10)$$

By analyzing the eigenvalues and eigenvectors of the Hessian matrix, the principal direction of the local structure can be extracted which is the direction of the smallest curvature (along the vessel). For an ideal tubular 3-D structure, the relationship between eigenvalues of the Hessian matrix is given by

$$\begin{aligned} |\lambda_3| \approx 0, \quad |\lambda_3| \ll |\lambda_2|, \quad \lambda_2 \approx \lambda_1 \quad \text{and} \\ (|\lambda_3| \leq |\lambda_2| \leq |\lambda_1|). \end{aligned} \quad (11)$$

Based on the second-order ellipsoid, three geometric ratios are defined

$$R_A = \frac{|\lambda_2|}{|\lambda_3|} \quad R_B = \frac{|\lambda_1|}{\sqrt{\lambda_2 \lambda_3}} \quad \text{and} \quad R_C = \|H\|_F = \sqrt{\sum_{j \leq D} \lambda_j^2}. \quad (12)$$

Here, R_A refers to the largest cross-section area of the ellipsoid that can distinguish between plate-like and line-like structures, R_B accounts for the deviation from a blob-like structure, and R_C is the Frobenius matrix that can distinguish background noise where no structures are present.

The vesselness function at scale s is defined as

$$v_0(s) = \begin{cases} 0 & \text{if } \lambda_2 > 0 \text{ or } \lambda_3 > 0 \\ \left(1 - e^{-\frac{R_A^2}{2\alpha^2}}\right) * e^{-\frac{R_B^2}{2\beta^2}} * \left(1 - e^{-\frac{R_C^2}{2\theta^2}}\right), & \end{cases} \quad (13)$$

where α , β , and θ are the thresholds which control the sensitivity of the line filter to the measures R_A , R_B , and R_C . The idea behind this expression is to map the features into probability-like estimates of vesselness according to different criteria.

The vesselness measure is analyzed at different scales. The response of the line filter will be maximum at a scale that approximately matches the vessel size

$$V_0(\gamma) = \arg \max_s v_0(s, \gamma), \quad s_{\min} < s < s_{\max}, \quad (14)$$

where s_{\min} and s_{\max} are the lower and upper bounds in the range of scale (vessel sizes).

3 Experimental Results

First, noninvasive baseline OCT/OMAG images were acquired from mouse ear pinna. Then, a 1-mm biopsy punch (Integra® Miltex®, Japan) was performed to remove tissue structures along one of the major artery/vein pairs of the ear. Then, OCT/OMAG images of the wound area were acquired immediately after punch. The wound area was monitored weekly for a few months until tissue was visually fully matured. Since the field-of-view of each OCT scan was limited to $\sim 2.2 \times 2.2 \text{ mm}^2$ (limited because of the numerical aperture of OCT objective lens), a total of nine images (3×3 overlapping scans) were acquired from the wound and its surrounding tissue structures to increase the field-of-view to $\sim 7 \times 7 \text{ mm}^2$. The imaging site was manually shifted using the mechanical stage and we allowed some overlap between adjacent scans for better stitching of individual images. The final image was generated by manually stitching individual images together to form a large field-of-view detailed image of blood flow perfusion and lymphatic vessels during the healing process. During different phases of the healing process, the following interesting observations were made.

3.1 Phase I: Hemostasis and Collateral Recruitment

After inducing the biopsy injury, a small amount of bleeding occurs at the injured site that immediately coagulates and fibrin blood clot is formed on the wound edge. The fibrin clot is formed due to aggregation and activation of platelets at the injury site. This is the first phase of the wound healing process. Just before the inflammatory phase, fibrin and fibronectin link together and form a net that prevents further blood loss by trapping proteins and particles.²⁵ The ear pinna in mice consists of a very dense and interconnected vascular network, and most of the adjacent arteries/veins are connected via anastomosis and collateral vessels. Immediately after cutting major artery/vein, blood flow circulation within the vascular network rewires due to formation of clot that blocks the vessel, variations of blood flow pressure within the vessels, and signaling pathways of cellular structures. Such rewiring of blood flow circulation allows the downstream tissues to survive. Figure 2 shows the blood flow perfusion maps before and immediately after the injury, respectively. The circle shows the location of biopsy punch and arrows indicate the collateral vessels that take

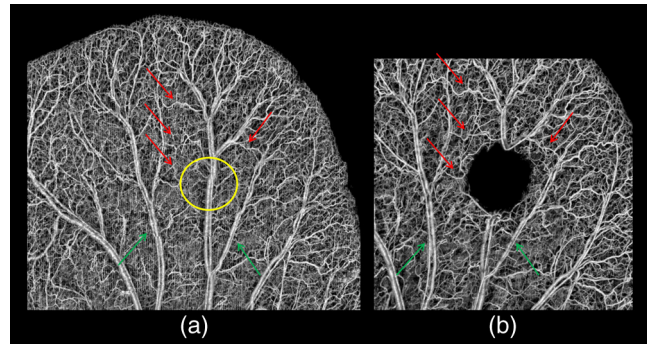


Fig. 2 (a) Before punch and (b) after punch. Collateral recruitment immediately after inducing the punch (circle). Collateral vessels indicated by arrows contribute to blood flow perfusion downstream to support blood flow. Green arrows: Collateral microvessels. Red arrows: shunts and bridges between the collaterals and downstream of the damaged tissue. Scale bar = 500 μm .

over the blood circulation in the downstream tissue. It can be observed that microcirculation rewiring happened immediately by utilizing the pre-existing vessels in the microvascular network. The green arrows indicate the collateral vessels that will support the damaged tissue immediately after inducing the injury. Also, the red arrows indicate the location of major shunts and bridges between the collaterals and the downstream microvessels. The blood supply is redirected through these channels immediately after the upstream major vessels are damaged. The vertical stripes on the baseline image are mainly due to animal motion artifact caused by involuntary respiratory and cardiac motion artifacts.

3.2 Phase II: Inflammation

Inflammation plays an important role in fighting infection, clearing debris, and inducing the proliferation phase in wound healing. Within a few hours, the second phase of wound healing (inflammation) starts when platelets release extracellular matrix (ECM) proteins, cytokines, and other proinflammatory factors into the blood. These factors increase cell proliferation and migration to the wound area and make blood vessels dilate.²⁶ Histamine is the factor that makes blood vessels dilate and become more porous. Increased vessel diameter and porosity facilitates the entry of inflammatory cells such as leukocytes into the wound site from the bloodstream.²⁷ Growth factors and fibronectin attract neutrophils to the wound site within a few hours of wounding to kill bacteria and cleanse the wound by secreting proteases that decompose damaged tissue. After completing their tasks, neutrophils undergo apoptosis and then are degraded by macrophages. Other leukocytes such as helper T-cells enter the wound site and secrete cytokines that increase inflammation and activity of macrophages.²⁸ Macrophages promote wound healing and regeneration by releasing factors that induce angiogenesis, re-epithelialization, formation of granulation tissue, and creation of new ECM and hence pushing the healing process into the next phase.²⁹

3.2.1 Dilatation of the collateral bridges

Although pre-existing collateral and anastomosis vessels help the downstream tissue to survive in the short term, hypoxic tissue is generated at the injury site and downstream. We observed that the recruited collateral bridges significantly enlarged with

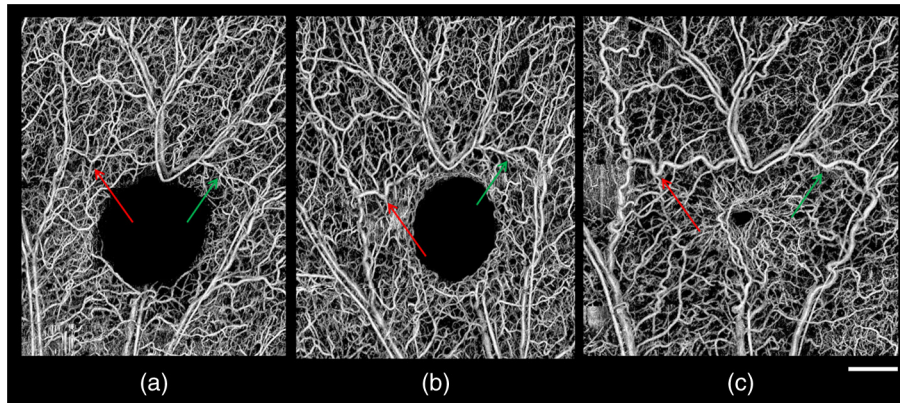


Fig. 3 (a) Immediate after punch, (b) 1 week, and (c) 7 weeks. Vasodilation in anastomosis shunt vessels. Red and green arrows indicate two shunt bridges from nearest collaterals. Scale bar = 500 μm .

time. Figure 3 show the enlargement of these bridges with time and arrows indicate the major bridges after injury. These changes mediate the increase of blood flow to support hypoxic tissue that requires increased blood supply to continue healing and surviving. During this phase, platelets at the wound site have released ECM proteins, growth, and proinflammatory factors such as histamine to the wound area and increased the diameter and porosity of collateral bridges.^{27,28}

Enlargement of vessels near hypoxic tissue was not limited to anastomosis bridges, and their upstream collateral vessels also enlarged significantly. Figure 4 shows dilation of the parallel collaterals that connect anastomosis bridges to the upstream blood supply. It was also observed that the enlargement of collateral vessels was accompanied by increase of their tortuosity, specifically for veins. Similar observations have been reported when vascular endothelial growth factor (VEGF) is utilized to trigger hypoxia-inducible factor-1 mediated neovascularization in gene knockout mice that lack VEGF.³⁰ We can explain our observation as follows: creating a biopsy punch can induce a hypoxic condition that triggers increase of growth factors including VEGF to the hypoxic area for wound healing and neovascularization. The increase in VEGF mediates enlargement of collateral and bridge vessels. At the same time, these vessels need to deliver more oxygen and nutrition supply via red blood cells to the damaged and hypoxic tissue, and their enlargement mediates that process.

3.2.2 Response of lymphatic vessels

The lymphatic system usually develops in parallel to the blood vessels in most internal organs or skin and is not present in the central nervous system, bone marrow, and avascular structures such as cartilage, epidermis, and cornea. In addition to draining lymph fluid from extracellular spaces, other roles of lymphatic system include absorbing lipids from intestinal tract, maintaining fluid hemostasis, and transporting antigen-presenting cells and leukocytes to lymphoid organs. Also, lymphatic system plays an important role in the development of several diseases such as cancer, lymphedema, some inflammatory conditions, and allergies.^{31–33}

Although no significant lymph was detected on the baseline image due to the limitation of the axial/spatial resolution, immediately after inducing the punch the lymphatic vessels were significantly enlarged around the wound and in the downstream tissue. Figure 5 shows the process of vasculature remodeling and lymphatic vessel response to the wound. Each image is composed of nine OCT-OMAG mosaics acquired around the wound area. Discontinuity of the blood and lymphatic vessel maps can be an artifact due to changes in optical angle and properties after shifting the stage. Blood vessels are orange-coded and lymphatic vessels were color-coded with green. The peak activity of lymphatic vessel enlargement was observed within ~ 1 week after inducing the wound. This observation is in

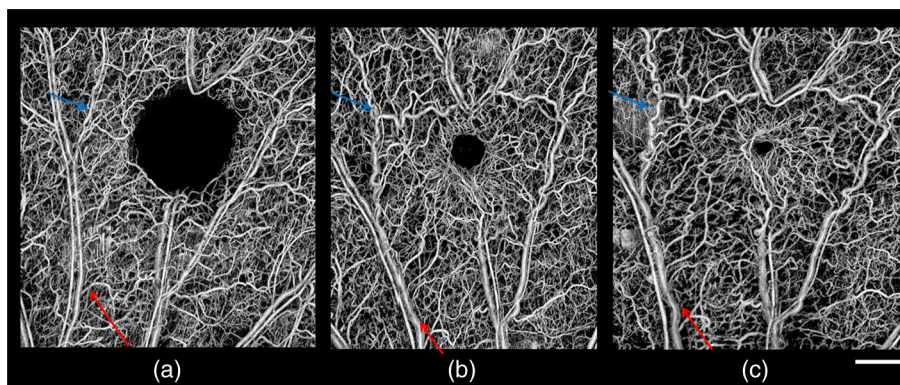


Fig. 4 (a) Immediate after punch, (b) 2 weeks, and (c) 7 weeks. Vasodilation in collateral vessels. The arrows indicate the collateral vessels that enlarge along the time to support the wound site. Scale bar = 500 μm .

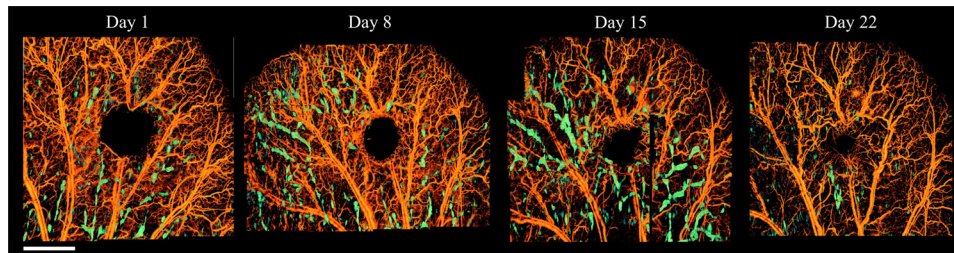


Fig. 5 Activity of lymphatic vessels during healing process along with blood flow perfusion map.

agreement with the wound healing phases during the inflammatory phase. The immediate response of lymphatic vessels after inducing the punch (Day 1) was mainly concentrated around the wound, collaterals, and downstream of the injured vessels. However, the size of the lymphatic vessels had significantly increased after 1 week (Day 8) and it was not only around the wound, but also at farther locations on the ear. Then, the size and distribution of lymphatic vessels were reduced after Day 22 and were mainly around the wound area due to inflammation.

3.3 Phase III: Proliferation

At the end of inflammatory phase, fewer inflammatory factors are secreted and a number of neutrophils and macrophages are reduced in the wound site.⁹ Inflammatory phase lasts as long as there is debris in the wound. Proliferation phase begins when endothelial cells migrate to the wound area and fibroblasts accumulate in the wound site, proliferate, and lay down collagen matrix as the inflammatory phase is ending. Fibroblasts are the main cells in the wound area by the end of first week and their number usually peaks at 1 to 2 weeks after injury. They usually originate from adjacent uninjured tissue and

circulating stem cells in the blood.³⁴ Fibroblasts utilize the fibrin crosslinking fibers to migrate across the wound and then deposit ground substance and collagen into the wound bed.¹⁶ Since the activity of fibroblasts and epithelial cells requires oxygen and nutrients, angiogenesis is necessary to support the healing process.³⁵ The fibronectin found in the fibrin scab attracts endothelial cells to the wound area. Stem cells of endothelial cells originating from parts of uninjured blood vessels develop pseudopodia and push through the ECM to the wound area and establish neovascularization.³⁶ Hypoxia and lactic acid in the wound area can directly stimulate endothelial growth and proliferation.³⁷

Figure 6 shows proliferation and angiogenesis in the wound area following the injury. The first row shows the microcirculation dynamics following the biopsy punch. Each image is generated by projecting the maximum intensity value of angiograms along the depth. Immediately after punch, injured capillaries and blood vessels coagulate and prevent tissue from bleeding. After 1 week, neovasculature within granulation tissue can be clearly observed that take the form of a “pile of woven wool.” After 2 weeks, wound contraction has already started pulling the neovasculature within the granulation tissue together and the “pile of wool” starts to open up. As the wound healing process

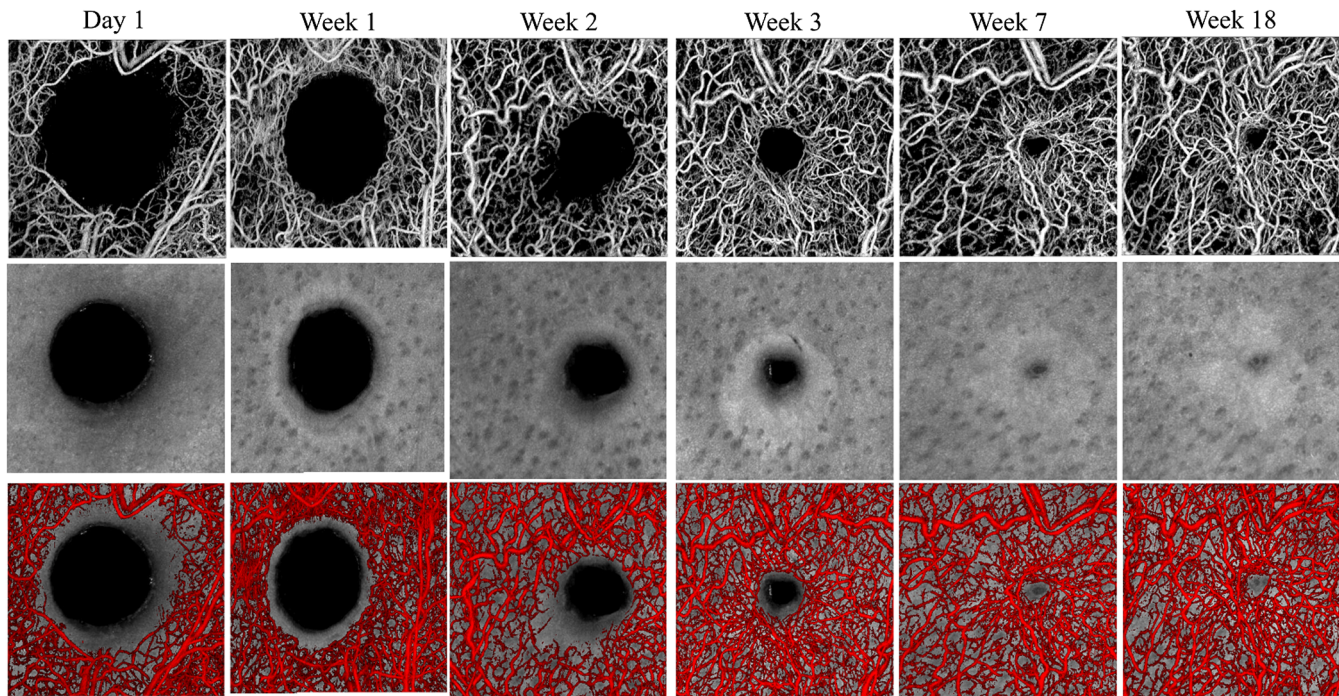


Fig. 6 Proliferation and neovascularization. Top row: maximum intensity projection map of blood flow perfusion. Middle row: average intensity projection of optical coherence tomography structure. Lower row: combined first and second rows, color-coded blood perfusion with red and the rest with gray.

continues toward the center of the wound, more granulation tissue is formed at the wound edges followed by neovascularization and angiogenesis. At maturation phase (around Week 18), some new vessels have grown larger while others have disappeared due to apoptosis.

In the second row of Fig. 6 is the average intensity projection of the structure OCT data that show structural changes during the healing process. The dark spots are hair follicles and the bright area around the wound location indicates proliferative activity of fibroblasts around the wound in fibrous matrix. The structure image also consists of some avascular regions in between the biopsy hole and the capillaries which its intensity value is lower than its surrounding vascular fibrous matrix. This region corresponds to the ECM and fibrin scabs that attract endothelial cells to the wound area and eventually promote proliferation and angiogenesis from existing blood vessels. In the third row of Fig. 6, we combined the maximum intensity projection maps from the first row (blood flow perfusion) with the second row (average intensity projection map) to show the location of vascular and avascular regions within the tissue.

Although OCT and OMAG technology cannot directly reveal the activity of endothelial cells and fibroblasts during proliferation phase, we can observe clues that lead us to such conclusions. The newly formed vessels within the first week after the injury provide oxygen and nutrition that supports the activity of fibroblasts (that lay down collagen matrix). Therefore, observing new blood vessels in the wound area are an indication of presence of endothelial cells and fibroblasts. In the future, the results should be validated by histology and direct labeling for further analysis and confirmation of our conclusions.

3.3.1 Re-epithelialization

Granulation tissue is a temporary structure consisting of neovasculature, inflammatory cells, endothelial cells, fibroblasts, myofibroblasts, and the components of a new provisional ECM that appears in the wound area during inflammatory phase.⁹ Fibroblasts produce collagen to increase the wound strength in addition to fibrin-fibronectin clot. Later on, cells involved in inflammation, angiogenesis, and connective tissue construction attach to grow and differentiate on the collagen matrix laid down by fibroblasts.³⁸ Re-epithelialization phase takes place when granulation tissue is formed in the wound area and epithelial cells migrate across the new tissue and form a barrier

between the wound and the external environment.³⁹ Basal keratinocytes at the wound edges and dermal appendages such as hair follicles and sweat glands are the main cells responsible for the epithelialization phase of wound healing.⁴⁰ Epithelialization advances across the wound edges and stops proliferation and movement when the wound edges meet each other in the middle. Epithelial cells grow like a sheet by climbing over each other to migrate (often called epithelial tongue).⁴¹ The first cells that attach to the basement membrane form the stratum basale that continue to migrate across the wound bed. Scar formation depends on how quick the epithelial cells migrate.⁴² Figure 7 shows the depth-encoded blood flow perfusion depth map around the wound and their corresponding tissue cross-section B-mode image. Epithelialization can be observed that advances across the wound edges, and proliferation stops when wound edges meet each other in the middle. Since epithelial cells grow by climbing over each other, wound edges always seem elevated compared to their distal structures and a scar tissue is formed around Week 7. Although the wound edges seem closed within 5 weeks and punch area is no longer see-through with naked eye, we can observe that the healing process inside the wound area continues for several months until tissue is fully matured.

3.3.2 Wound contraction

Wound contraction is defined as the movement of wound edges toward the center to close it. During wound contraction, fibrous tissue starts to form inside the wound and pulls the boundaries of the injury together.¹ The closure of the wound protects underlying tissues and prepares for maturation phase. In cutaneous wound healing, signs of wound contraction are changes in color, itchiness, and obvious reduction in wound size. If the wound shape is circular, the healing process seems irregular because the skin is pulled together irregularly due to contraction. In most cases, contraction occurs asymmetrically around an axis of contraction that allows better alignment of cells with collagen.⁴³ Myofibroblasts that contain the same kind of actin found in smooth muscle cells are responsible for wound contraction. Although contraction starts without myofibroblast involvement at first, myofibroblasts are differentiated from growth factor stimulated fibroblasts. Then, myofibroblasts are attracted by fibronectin and growth factors in the ECM to reach and attach to the wound edges and collagen by desmosomes that allow

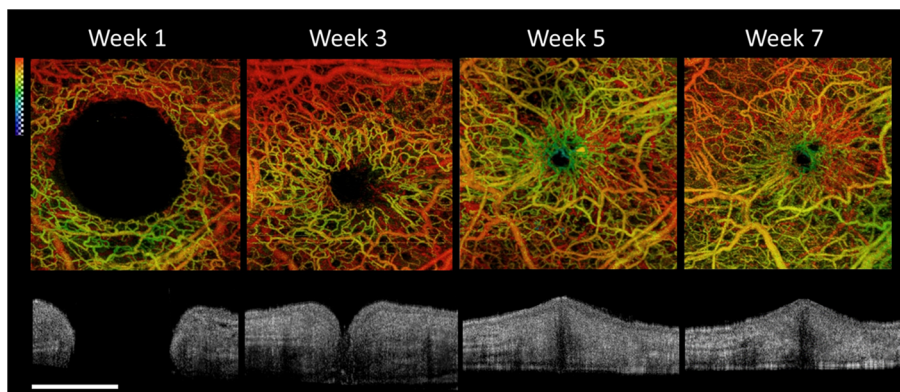


Fig. 7 Epithelialization. Depth-encoded en-face maximum intensity projection of blood flow perfusion around wound around and their corresponding structure cross-section images during epithelialization phase. Red color indicates deeper and blue color indicates more shallow vessels and green color is in between. Initial wound diameter on Week 1 is around 1 mm.

them to pull the ECM when they contract.⁴⁴ As provisional matrix breaks down, hyaluronic acid decreases while chondroitin sulfate increases and gradually triggers fibroblasts to stop proliferating. These events signal the end of contraction stage and beginning of maturation phase.⁴⁵ In hospital settings, the wound is kept clean and dry during this phase of healing to prevent severe injuries such as infection, contracture, and a failure to fully close. Contraction is considered as a good sign that indicates wound healing is moving toward maturation and the patient will be sent home soon.

Figure 8 shows wound contraction during healing after biopsy punch. It can be observed that contraction around the third week is pulling the edges at an irregular shape and wound size is reduced by the fourth week due to wound contraction and angiogenesis. As the healing process enters the maturation phase, contraction decreases, and blood vessels within ECM separate and become more distinct.

3.4 Maturation and Remodeling after Wound Closure

Maturation phase of wound healing begins when the levels of collagen production and degradation have equalized.¹ During maturation, disorganized collagen fibers are rearranged and aligned along tension lines, and type III collagen is replaced by type I collagen.⁴⁶ Depending on the wound type, maturation phase can last for a year or more, leading to a permanent scar left behind. Since activity of the wound site is reduced and the blood vessels that are no longer needed are removed by apoptosis, the scar redness is reduced, and the tensile strength of the wound gradually increases.³⁶ Figure 9 shows the maturation process and remodeling in the wound model. Although by the 36th day, the wound site has fully closed, maturation and remodeling continues for a long time and might take several months.

4 Discussion

Although wound healing models in rodents are very attractive because of their availability, ease of handling, and low cost, they are criticized for not mimicking the healing mechanism in human wounds. In humans, the major mechanisms of wound closure are re-epithelialization and granulation tissue formation, while in rodents they are contraction. In order to minimize the wound contraction, accurate wound splitting can be performed.⁴⁷ Due to the differences between human and rodent skin, pig skin can be a better model of wound healing because of its similarity to the human.⁴⁸ Both human and pig skin have a thick epidermis (~ 50 to $100 \mu\text{m}$),⁴⁹ show well-developed rete-ridges and dermal papillary bodies and abundant subdermal adipose tissue,^{50–52} similar elasticity,⁵³ similar dermis microvasculature pattern,^{54–56} and sparse body hair that unlike many animals, profuses through the hair cycle independently of neighboring follicles.⁵²

Although we have shown qualitative assessment of our wound healing model, multiple parameters can be quantified such as diameter of the blood vessels, lymphatic vessels, and the connection of microcirculatory system. However, accurate estimation of angiogram diameter requires similar experimental conditions. Since we monitor and image our model for ~ 8 weeks or more, in every experiment, we have to make sure that the placement is identical from one experiment session to another. For instance, the objective lens that we utilized is considered a high numerical aperture ($10\times$) and therefore depth of focus (DOF) is limited to a few hundreds of microns in the tissue. In order to keep the experimental placements similar, we have to make sure that each imaging is performed from the exact DOF in the ear while the ear tissue is very flexible, and such a claim can never be true. The ear tissue is not entirely flat and its thickness and shape varies from location to location. In order to quantify the exact diameter of the blood/lymphatic

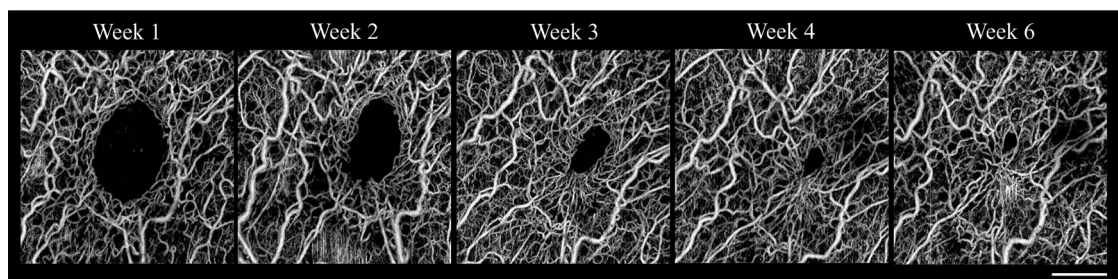


Fig. 8 Wound contraction. Scale bar = $500 \mu\text{m}$.

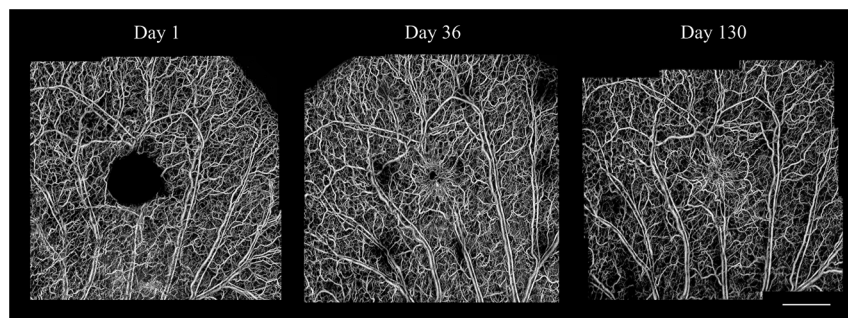


Fig. 9 Maturation and remodeling. Scale bar = 1 mm .

vessels, one has to make sure to take all of these limitations into account. If the ear tissue is placed $\sim 100 \mu\text{m}$ above or below the previous location of its placement in the previous experiment, the quantified vessel diameter encodes an error and this error may not be consistent from time to time. Unless consistent and repeatable variations happen, no one can hypothesize and relate any conclusions based on the estimated parameters on OMAG images in the wound healing model. One way to overcome these limitations is by dynamic focusing and spatial compounding multiple OCT scans for each spatial location and then combining results to reconstruct long DOF OCT angiograms. Another solution is by modeling the depth-dependent beam broadening of the system and performing inverse model reconstruction of the OCT signal. Since the ear model consists of a cartilage in the middle, that cartilage layer can be utilized as a reference to adjust the best focus location within the ear tissue. After correcting for spatial defocusing, blood vessels can be quantified by segmenting their location from background, quantifying their diameter, and other parameters such as vessel area density and tortuosity.⁵⁷

Another limiting factor of quantification of blood vessels is the signal ambiguity below the blood vessels because of multiple and forward scattering of photons by red blood cells. In that case, a shadow is cast below the blood vessels and angiograms appear as blood vessels with a long tail. The shadow and tail artifact can cause confusion and error when quantifying blood vessels and therefore a shadow-correction should be utilized.⁵⁸ Also, attenuation coefficient in the ear tissue can change in between the healing phases, and tissue swelling and inflammation changes the optical properties of the tissue. Accurate quantification of the healing process requires an estimate of the variations based on tissue properties and a correction factor should be applied.⁵⁹

Wound size can be quantified to compare the healing process in different samples. However, our wound model is not supported by muscle substrates below them and therefore wound contraction can cause error in the quantification of healing process. Also, the closure itself cannot be a very good way to relate to the healing process because as we have shown in this paper, maturation phase can take a very long time and better healing is followed by better vascularization and angiogenesis, as well as the quality of the neovascularization within the granulation tissue.

OCT modality is based on the scanning laser and cannot be considered as a true real-time imaging modality. If a phenomenon is of interest to be monitored/quantified, other modalities such as laser speckle imaging (LSI) can be utilized to monitor wound healing in the whole ear tissue.⁶⁰ The tradeoff is that LSI cannot reveal depth information and structural cross section and the resolution of LSI is above the size of single capillary. Although OCT is almost-real time, it provides depth-resolved and capillary-resolution information and therefore a combination of OCT and LSI can be a powerful tool to assess wound healing in tissue samples.⁶¹ The observed lymphatic vessels on the OCT structure images are directly related to the resolution of the system. By increasing the system resolution, smaller lymphatic vessels and capillaries can also be observed, which can be segmented using our proposed method. Since the axial resolution of the system is directly related to the spectral bandwidth of the light source, utilizing laser light sources with broader bandwidth can enhance the resolution of the system and therefore the quality of the observed lymphatic vessel could enhance dramatically.

We should note that OCT/OMAG technology is not sensitive to detecting cytokines, proinflammatory factors, and growth factors that are released during the wound healing process. However, given the prior knowledge of their role during wound healing process, we could infer from our observations that what might have happened. Again, these are scientific conclusions and of course *in vivo* validation requires further studies.

Angiography imaging using OCT has been demonstrated in the literature for imaging structure and microcirculation in human finger cuticle,⁶² subcutaneous,⁶³ and fingertip.⁶⁴ Also, other techniques such as laser speckle have been demonstrated for label-free noninvasive simultaneous imaging blood and lymphatic vessels in the mouse ear pinna model.⁶⁵ Since each of these modalities provides complementary information, they can be combined in future for further analysis of healing models and tailoring therapeutic strategies in wound healing⁶⁶ and tumor angiogenesis.⁶⁷

Recently, OCT imaging has been utilized to demonstrate the capability of this technology to characterize and monitor cutaneous wound-healing phases in human leg ulcers⁶⁸ and volunteers.⁶⁹ The results were in agreement with the histological staining of the same tissue structure and therefore, OCT structural and microcirculatory information can be utilized as a label-free noninvasive tool to assess and monitor wound healing in animal models and human.

5 Conclusions

Cutaneous wound healing consists of several overlapping phases including hemostasis, inflammation, tissue formation, and tissue remodeling. In this paper, we utilized OCT/OMAG to noninvasively monitor the wound healing dynamic process in mouse ear pinna model *in vivo*. The high-resolution OMAG allows tracking microvascular details up to capillary level. Our results are in agreement with expected behavior of tissue during wound healing stages, and we can conclude that OCT/OMAG proves to be a practical tool for tracking wound healing in a mouse model. In the future, we would like to generalize our results to human studies to design treatment strategies for burns, chronic skin ulcers, and diabetes mellitus.

Acknowledgments

This work was supported in part by research grants from the National Institutes of Health (R01EB009682 and R01HL093140). The funders had no role in study design, data collection and analysis, decision to publish, or preparation of this paper.

References

1. A. J. Singer and R. A. Clark, "Cutaneous wound healing," *New Engl. J. Med.* **341**(10), 738–746 (1999).
2. J. H. Barker et al., "The hairless mouse ear for *in vivo* studies of skin microcirculation," *Plast. Reconstr. Surg.* **83**(6), 948–959 (1989).
3. E. Eriksson, J. V. Boykin, and R. N. Pittman, "Method for *in vivo* microscopy of the cutaneous microcirculation of the hairless mouse ear," *Microvasc. Res.* **19**(3), 374–379 (1980).
4. P. H. Tomlins and R. K. Wang, "Theory, developments and applications of optical coherence tomography," *J. Phys. D* **38**(15), 2519–2535 (2005).
5. A. Fercher et al., "Optical coherence tomography-principles and applications," *Rep. Prog. Phys.* **66**(2), 239–303 (2003).
6. R. K. Wang et al., "Three dimensional optical angiography," *Opt. Express* **15**(7), 4083–4097 (2007).

7. R. K. Wang and S. Hurst, "Mapping of cerebro-vascular blood perfusion in mice with skin and skull intact by optical micro-angiography at 1.3 μm wavelength," *Opt. Express* **15**(18), 11402–11412 (2007).
8. H. M. Subhash et al., "Volumetric *in vivo* imaging of microvascular perfusion within the intact cochlea in mice using ultra-high sensitive optical microangiography," *IEEE Trans. Med. Imaging* **30**(2), 224–230 (2011).
9. W. J. Choi, H. Q. Wang, and R. K. Wang, "OCT microangiography for monitoring the response of vascular perfusion to external pressure on human skin tissue," *J. Biomed. Opt.* **19**(5), 056003 (2014).
10. E. Jonathan, J. Enfield, and M. J. Leahy, "Correlation mapping method for generating microcirculation morphology from optical coherence tomography (OCT) intensity images," *J. Biophotonics* **4**(9), 583–587 (2011).
11. W. J. Choi et al., "Improved microcirculation imaging of human skin *in vivo* using optical microangiography with a correlation mapping mask," *J. Biomed. Opt.* **19**(3), 036010 (2014).
12. Y. Jia et al., "Split-spectrum amplitude-decorrelation angiography with optical coherence tomography," *Opt. Express* **20**(4), 4710–4725 (2012).
13. R. Reif et al., "Analysis of cross-sectional image filters for evaluating nonaveraged optical microangiography images," *Appl. Opt.* **53**(5), 806–815 (2014).
14. S. Yousefi, Z. Zhi, and R. K. Wang, "Eigendecomposition-based clutter filtering technique for optical microangiography," *IEEE Trans. Biomed. Eng.* **58**(8), 2316–2323 (2011).
15. P. V. Peplow, T. Y. Chung, and G. D. Baxter, "Laser photobiomodulation of wound healing: a review of experimental studies in mouse and rat animal models," *Photomed. Laser Surg.* **28**(3), 291–325 (2010).
16. S. Werner and R. Grose, "Regulation of wound healing by growth factors and cytokines," *Physiol. Rev.* **83**(3), 835–870 (2003).
17. Y. Jung et al., "Tracking dynamic microvascular changes during healing after complete biopsy punch on the mouse pinna using optical microangiography," *PLoS One* **8**(2), e57976 (2013).
18. A. Rege et al., "*In vivo* laser speckle imaging reveals microvascular remodeling and hemodynamic changes during wound healing angiogenesis," *Angiogenesis* **15**(1), 87–98 (2012).
19. L. Shi et al., "Wide velocity range Doppler optical microangiography using optimized step-scanning protocol with phase variance mask," *J. Biomed. Opt.* **18**(10), 106015 (2013).
20. R. K. Wang et al., "Depth-resolved imaging of capillary networks in retina and choroid using ultrahigh sensitive optical microangiography," *Opt. Lett.* **35**(9), 1467–1469 (2010).
21. R. K. Wang and Z. Ma, "A practical approach to eliminate autocorrelation artifacts for volume-rate spectral domain optical coherence tomography," *Phys. Med. Biol.* **51**(3), 3231–3239 (2006).
22. H. Stark and J. W. Woods, *Probability, Random Processes, and Estimation Theory for Engineers*, 3rd ed., pp. 139–142, Prentice-Hall, Englewood Cliffs, NJ (1986).
23. S. Yousefi, Z. Zhi, and R. K. Wang, "Label-free optical imaging of lymphatic vessels within tissue beds *in vivo*," *IEEE J. Sel. Top. Quantum Electron.* **20**(2), 6800510 (2014).
24. S. Yousefi et al., "Label-free optical lymphangiography: development of an automatic segmentation method applied to optical coherence tomography to visualize lymphatic vessels using Hessian filters," *J. Biomed. Opt.* **18**(8), 086004 (2013).
25. S. V. Mallett and D. J. A. Cox, "Thrombelastography," *Br. J. Anaesth.* **69**(3), 307–313 (1992).
26. R. Raghov, "The role of extracellular matrix in postinflammatory wound healing and fibrosis," *FASEB J.* **8**(11), 823–831 (1994).
27. J. F. Boyd and A. N. Smith, "The effect of histamine and a histamine-releasing agent (compound 48/80) on wound healing," *J. Pathol. Bacteriol.* **78**(2), 379–388 (1959).
28. R. Gillitzer and M. Goebeler, "Chemokines in cutaneous wound healing," *J. Leukocyte Biol.* **69**(4), 513–521 (2001).
29. D. A. Rappolee et al., "Wound macrophages express TGF- α and other growth factors *in vivo*: analysis by mRNA phenotyping," *Science* **241**(4866), 708–712 (1988).
30. S. Oladipupo et al., "VEGF is essential for hypoxia-inducible factor-mediated neovascularization but dispensable for endothelial sprouting," *Proc. Natl. Acad. Sci. U. S. A.* **108**(32), 13264–13269 (2011).
31. K. Alitalo, T. Tammela, and T. V. Petrova, "Lymphangiogenesis in development and human disease," *Nature* **438**(7070), 946–953 (2005).
32. G. Oliver, "Lymphatic vasculature development," *Nat. Rev. Immunol.* **4**(1), 35–45 (2004).
33. S. Zraggen, A. M. Ochsenbein, and M. Detmar, "An important role of blood and lymphatic vessels in inflammation and allergy," *J. Allergy* **2013**, 672381 (2013).
34. G. Song et al., "Use of the parabiotic model in studies of cutaneous wound healing to define the participation of circulating cells," *Wound Repair Regen.* **18**(4), 426–432 (2010).
35. M. G. Tonnesen, X. Feng, and R. A. Clark, "Angiogenesis in wound healing," *J. Invest. Dermatol. Symp. Proc.* **5**(1), 40–46 (2000).
36. D. G. Greenhalgh, "The role of apoptosis in wound healing," *Int. J. Biochem. Cell Biol.* **30**(9), 1019–1030 (1998).
37. V. Falanga, "Wound healing and its impairment in the diabetic foot," *Lancet* **366**(9498), 1736–1743 (2005).
38. Z. Ruzszzak, "Effect of collagen matrices on dermal wound healing," *Adv. Drug Deliv. Rev.* **55**(12), 1595–1611 (2003).
39. H. Larjava, L. Häkkinen, and L. Koivisto, "Re-epithelialization of wounds," *Endoscopic Topics* **24**(1), 59–93 (2012).
40. L. A. DiPietro, "Wound healing: the role of the macrophage and other immune cells," *Shock* **4**(4), 233–240 (1995).
41. J. Bartkova et al., "Cell-cycle regulatory proteins in human wound healing," *Arch. Oral Biol.* **48**(2), 125–132 (2003).
42. H. J. Son et al., "Effects of β -glucan on proliferation and migration of fibroblasts," *Curr. Appl. Phys.* **5**(5), 468–471 (2005).
43. M. J. Eichler and M. A. Carlson, "Modeling dermal granulation tissue with the linear fibroblast-populated collagen matrix: a comparison with the round matrix model," *J. Dermatol. Sci.* **41**(2), 97–108 (2006).
44. U. Miratschijski et al., "Matrix metalloproteinase inhibitor GM 6001 attenuates keratinocyte migration, contraction and myofibroblast formation in skin wounds," *Exp. Cell Res.* **299**(2), 465–475 (2004).
45. B. Hinz, "Masters and servants of the force: the role of matrix adhesions in myofibroblast force perception and transmission," *Eur. J. Cell Biol.* **85**(3–4), 175–181 (2006).
46. K. Vanderwee et al., "Pressure ulcer prevalence in Europe: a pilot study," *J. Eval. Clin. Pract.* **13**(2), 227–235 (2007).
47. R. D. Galiano et al., "Quantitative and reproducible murine model of excisional wound healing," *Wound Repair Regen.* **12**(4), 485–492 (2004).
48. T. P. Sullivan et al., "The pig as a model for human wound healing," *Wound Repair Regen.* **9**(2), 66–76 (2001).
49. W. Meyer, R. Schwarz, and K. Neurand, "The skin of domestic mammals as a model for the human skin with special reference to the domestic pig," *Curr. Probl. Dermatol.* **7**, 39–52 (1978).
50. G. M. Morris and J. W. Hopewell, "Epidermal cell kinetics of the pig: a review," *Cell Tissue Kinet.* **23**(4), 271–282 (1990).
51. W. Montagna and J. S. Yun, "The skin of the domestic pig," *J. Invest. Dermatol.* **43**(1), 11–21 (1964).
52. G. D. Winter, "A study of wound healing in the domestic pig," Ph.D. Thesis, Birbeck College, University of London, UK (1966).
53. H. Q. Marcarian and M. L. Calhoun, "Microscopic anatomy of the integument of adult swine," *Am. J. Vet. Res.* **27**(118), 765–772 (1966).
54. P. D. Forbes, "Vascular supply of the skin and hair in swine," in *Advances in the Biology of the Skin*, 9th ed., p. 419, Pergamon, New York (1969).
55. J. Rothenberger et al., "Development of an animal frostbite injury model using the Goettingen-Minipig," *Burns* **40**(2), 268–273 (2014).
56. A. R. Mortite and F. C. Henriques, "Studies of thermal injury II. The relative importance of time and surface temperature in the causation of cutaneous burns," *Am. J. Pathol.* **23**(5), 695–720 (1947).
57. R. Reif et al., "Quantifying optical microangiography images obtained from a spectral domain optical coherence tomography system," *Int. J. Biomed. Imaging* **2012**, 509783 (2012).
58. M. Girard et al., "Shadow removal and contrast enhancement in optical coherence tomography images of the human optic nerve head," *Invest. Ophthalmol. Vis. Sci.* **52**(10), 7738–7748 (2011).
59. K. A. Vermeer et al., "Depth-resolved model-based reconstruction of attenuation coefficients in optical coherence tomography," *Biomed. Opt. Express* **5**(1), 322–337 (2014).
60. A. Rege et al., "*In vivo* laser speckle imaging reveals microvascular remodeling and hemodynamic changes during wound healing angiogenesis," *Angiogenesis* **15**(1), 87–98 (2012).
61. R. Reif et al., "Monitoring hypoxia induced changes in cochlear blood flow and hemoglobin concentration using a combined dual-wavelength

- laser speckle contrast imaging and Doppler optical microangiography system," *PLoS One* **7**(12), e52041 (2012).
62. U. Baran, L. Shi, and R. K. Wang, "Capillary blood flow imaging within human finger cuticle using optical microangiography," *J. Biophotonics*, 1–6 (2013).
 63. A. Doronin and I. Meglinski, "Imaging of subcutaneous microcirculation vascular network by double correlation optical coherence tomography," *Laser Photonics Rev.* **7**(5), 797–800 (2013).
 64. R. I. Dsouza et al., "In vivo microcirculation imaging of the sub surface fingertip using correlation mapping optical coherence tomography (cmOCT)," *Proc. SPIE* **8580**, 85800M (2013).
 65. V. Kalchenko et al., "Label free *in vivo* laser speckle imaging of blood and lymph vessels," *J. Biomed. Opt.* **17**(5), 050502 (2012).
 66. H. Wang et al., "Multimodal optical imaging can reveal changes in microcirculation and tissue oxygenation during skin wound healing," *Lasers Surg. Med.* (2014).
 67. V. Kalchenko et al., "In vivo characterization of tumor and tumor vascular network using multi-modal imaging approach," *J. Biophotonics* **4**(9), 645–649 (2011).
 68. M. Kuck et al., "Evaluation of optical coherence tomography as a non-invasive diagnostic tool in cutaneous wound healing," *Skin Res. Technol.* **20**(1), 1–7 (2014).
 69. N. S. Greaves et al., "Optical coherence tomography: a reliable alternative to invasive histological assessment of acute wound healing in human skin?," *Br. J. Dermatol.* **170**(4), 840–850 (2013) (in press).

Biographies of the authors are not available.